21st Australasian Fluid Mechanics Conference
Adelaide, Australia
10-13 December 2018

Low Reynolds number turbulent swirling pipe flows

R. C. Chin[1] and J. Philip[2]

[1]School of Mechanical Engineering
Adelaide University, SA - 5005, Australia

[2]Department of Mechanical Engineering
The University of Melbourne, VIC - 3010, Australia

Abstract

A direct numerical simulation of a swirling pipe flow is performed to investigate the effects of swirl on turbulence statistics. The swirling motion is imposed via a constant azimuthal body force coupled with a body force in the axial direction that drives the flow. The friction Reynolds number $Re_\tau \approx 170$ with a pipe length of $8\pi\delta$ (where δ is the pipe radius). The simulations are performed at two swirl numbers $S = 0.01$ and 0.13. At the lower swirl number, the mean statistics appear to collapse well with non-swirling pipe flows. At the higher swirl number, the axial, radial and azimuthal turbulence intensities show a higher value in the outer region, whereas the axial turbulence intensity decreases closer to the wall. The higher swirl number simulation shows that there is an increase in drag, possibly due to the swirl imposing an increase in axial flow resistance. This is accompanied by an increase in the inertial region with increased swirl. We also show that similar to the total axial stress, the total azimuthal stress when normalised by the azimuthal friction velocity follows decreases linearly from wall to the pipe centerline.

Introduction

Swirling flow in a confined region has many engineering applications; however, here we are motivated by two specific cases: (i) combustion chambers — where the incoming flow is swirled to stabilize the flame; and (ii) transport and separation in particle laden flows — where swirling flow in a pipe can centrifugally separate the particles due to their higher density compared to the fluid. In the present paper we have idealised the scenario, and carry out direct numerical simulation (DNS) of incompressible turbulent pipe flows, wherein apart from the usual mean streamwise velocity (U_x) we also have a mean azimuthal velocity (U_θ). Here, (x, r, θ) represent the cylindrical co-ordinates and ($\tilde{u}_x$, $\tilde{u}_r$, $\tilde{u}_\theta$) the instantaneous velocities in the corresponding direction, which are decomposed into (x,θ)-averaged mean and fluctuations, e.g., $\tilde{u}_x = U_x + u_x$. For mean quantities, we use either capital letter (e.g., U_x) or angled-brackets (e.g., $\langle u_x u_r \rangle$).

Swirling turbulent pipe flows

The are two distinct ways (both experimentally and numerically) in which swirl can be imposed on a usual turbulent pipe flow. (i) The pipe wall is rotated, which results in a maximum azimuthal velocity at the wall (e.g., [4, 5, 7, 8]), and produces a swirl that is *centripetal* in nature[6]. (ii) The pipe is held stationary, and a swirling flow is introduced at the inlet using vanes or tangential jets into the pipe. Here, the azimuthal component of the velocity slowly decays with the downstream distance, and in the radial direction the maximum azimuthal velocity is somewhere between the wall and the centreline (e.g., [9, 10, 6]). This is a more practical method used in industry, and is referred to as *centrifugal* in nature[6]. In this paper, motivated by practical applications, we adopt the second method. Details of the simulation method and swirl implementation will be presented in the next section.

Introduction of high swirl to an otherwise regular turbulent pipe flow has stabilising effects, and researchers have observed a reduction in the net drag (e.g., [4]), whereas there is some evidence of increased drag at low swirl strengths (e.g., [11]). We note that for simplicity most studies have focused on a rotating pipe rather than the stationary pipe with swirling flow. As such, there is a paucity of data for swirling flows in stationary pipes, and the present work is a first step in understanding the turbulent flow behaviour in such scenarios.

Inertial regime of non-swirling turbulent pipe flows

Of the many interesting aspects that a turbulent pipe flow (or any wall turbulent flow) exhibits, the one which has received considerable attentions in recent years is the region where the flow shows an inertial behaviour (e.g., [12]). Inertial region is defined as the wall-normal distance over which the viscous force (VF) in the mean momentum equation (c.f., equation (1)) is negligible compared to the pressure gradient (PG) and turbulent inertia (TI):

$$\underbrace{\frac{\mathrm{d}\langle -u_x v\rangle^+}{\mathrm{d}y^+}}_{\mathbf{TI}} + \underbrace{\frac{\mathrm{d}^2 U_x{}^+}{\mathrm{d}y^{+2}}}_{\mathbf{VF}} + \underbrace{\frac{1}{\delta^+}}_{\mathbf{PG}} = 0. \qquad (1)$$

Here we have replaced $u_r \mapsto -v$ and $y := \delta - r$, where δ is the pipe radius, and the '+' symbol denotes scaling with viscous units $u_{\tau,x}$ (the x-direction friction velocity $= \sqrt{\nu\, \mathrm{d}U_x/\mathrm{d}y|_{y=0}}$) and ν (the kinematic viscosity). The start of this inertial regime, or location where U_x starts exhibiting a log-profile has been a contentious issue. However, now it is clear both from experiments and analysis (e.g., [13, 14, 15]) that the inertial region starts at $C\sqrt{\delta^+}$, where C is an $O(1)$ constant (≈ 2.8 for pipe flows), and differs between canonical wall turbulent flow. It is not clear how the inertial regime moves with the inclusion of swirl. As such, here we aim to present some preliminary simulations with two different swirl strengths (to be defined later), and characterise the flow inertial regime using (1), which is valid also for our swirling flow cases. Although, we think that the $Re_\tau = \delta^+ \approx 170$ for the present simulations is lower that what we would prefer to have a clear distinction of the inertial regime, the ideas presented here are applicable for higher δ^+ cases, which are currently being run.

Swirl generation and the numerical method

We intend to simulate a scenario wherein once the swirling flow enters the pipe, it is in an 'equilibrium' condition ([10]), i.e., the swirl strength is constant and does not decay downstream. This is a reasonable assumption if we consider a section of the pipe that is short compared to the distance over which swirl decays. The axially and azimuthally averaged mean axial and azimuthal

Case	P0	P5	P50
Re_τ	170	170	170
f_θ	$0f_x$	$0.05f_x$	$0.5f_x$
L_x	$8\pi\delta$	$8\pi\delta$	$8\pi\delta$
Δx^+	6.7	6.7	6.7
Δr^+	[0.5, 3.6]	[0.5, 3.6]	[0.5, 3.6]
$\Delta r\theta^+$ (at wall)	8.4	8.4	8.4
S	0	0.01	0.13

Table 1: Summary of numerical simulation parameters.

momentum equations are[10]:

$$\frac{1}{r}\frac{\mathrm{d}}{\mathrm{d}r}(r\tau_{xr}) + f_x = 0, \text{ and, } \frac{1}{r}\frac{\mathrm{d}}{\mathrm{d}r}(r\tau_{r\theta}) + \frac{\tau_{r\theta}}{r} + f_\theta = 0, \qquad (2)$$

where, the total stresses (per unit density) $\tau_{xr} = \nu\frac{\mathrm{d}U_x}{\mathrm{d}r} - \langle u_r u_x\rangle$, and $\tau_{r\theta} = \nu\left(\frac{\mathrm{d}U_\theta}{\mathrm{d}r} - \frac{U_\theta}{r}\right) - \langle u_r u_\theta\rangle$. Here, f_x is the forcing in x equal to the constant axial pressure gradient (per unit density), and f_θ is the azimuthal forcing, given by $f_\theta = af_x$, whereby a is a percentage of f_x. (Also, see [10] for a comparison of different kinds of forcing, $f_\theta(r)$.) The swirl number S is the ratio of the axial fluxes of the azimuthal to axial momentum defined as,

$$S = \frac{\int \rho\overline{\tilde{u}_x\tilde{u}_r}r^2\mathrm{d}r\mathrm{d}\theta}{R\int \rho\overline{\tilde{u}_x^2}r\mathrm{d}r\mathrm{d}\theta}. \qquad (3)$$

The numerical scheme employed to perform the pipe flow simulations is detailed in [1]. The numerical scheme has been validated for pipe flows in [2]. The scheme uses a spectral element discretisation in the meridional semi-plane with a 11^{th} order Gauss-Lobatto-Legendre nodal-based expansion in each element and a Fourier discretisation in the azimuthal direction. The axial, radial and azimuthal directions have N_x, N_r and N_θ number of elements. A periodic boundary condition is specified in the axial direction for the inlet and outlet of the pipe. The fluid flow in the axial direction is driven by a body force defined as f_x and f_θ. The f_x utilised in the simulation corresponds to a friction Reynolds number of $Re_\tau \approx 170$. To perform the swirling pipe flow simulations, fully developed turbulent pipe flow data from [3] is utilised to start the simulation.

The details of the computational domains for both Reynolds numbers are summarised in table 1. The spatial resolutions and domain length are kept constant for each case.

Results

Flow visualisation and mean velocity profiles

Here we carry out three different simulations, corresponding to $a = 0\%$ (no forcing, **P0**), 5% (**P5**) and 50% (**P50**) forcing. Figure 1 shows the contours of $\tilde{u_x}$ close to the wall at $y^+ \approx 15$ for the three cases. The near wall streaks with the azimuthal spacing of ≈ 100 viscous units are clearly visible in figure 1(a) for no forcing, whereas the streaks start to tilt with increasing a to about a slope of $1/4$ with 50% forcing. Similar results are observed by others (e.g., [10, 11]) too. Comparing the three panels in figure 1 shows that the streaks are getting 'thicker' and perhaps longer with increasing swirl strength a. A spectral analysis (to be carried out in future) would best elucidate this point.

The velocity distribution over the pipe cross section for different the three cases are presented in figure 2, where a reduced axial flow is observed for $a = 50\%$ (**P50**). This feature is best

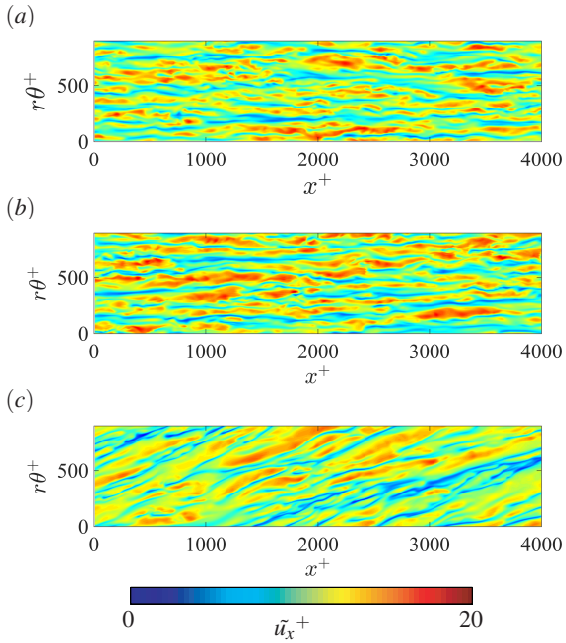

Figure 1: Instantenous axial velocity in the $x-r\theta$ plane for all cases at wall-normal location $y^+ \approx 15$. (a) non-swirling pipe **P0**, (b) 5% forcing **P5** and (c) 50% forcing **P50**.

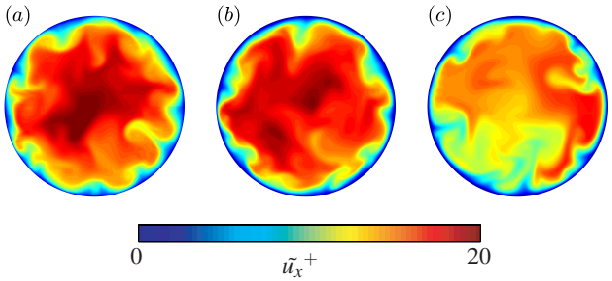

Figure 2: Instantenous axial velocity profile. (a) non-swirling pipe **P0**, (b) 5% forcing **P5** and (c) 50% forcing **P50**.

observed in the profiles of $U_x{}^+(r)$ shown in figure 3, which clearly shows a reduced centreline velocity for the 50% forcing (blue line). Not surprisingly, the distribution of $U_\theta{}^+$ (in figure 4) shows an increased azimuthal velocity for increased azimuthal forcing f_θ. Interestingly, the ratio of the maximum azimuthal and axial velocity for case **P50** is $\approx 3.5/14$, which is close to the $\approx 1/4$ slope of the streak angle that is observed. As such, it seems that the streaks are simply tilted by the corresponding velocities; although it does not explain the structural changes to the streaks themselves.

Another important point from figure 3 is that the bulk velocity decreases with increasing a (at least till 50% forcing). We recall that the forcing f_x is fixed in all cases. This suggests that the flow *feels* more obstruction with increasing swirl strength, and although the axial drag is the same (i.e., same δ^+) for all forcing, the flow might show some features of a 'more turbulent' flow. In fact, this manifests itself in the analysis of the equation (1) later.

Reynolds stresses

Figure 5 shows the three normal Reynolds stresses (e.g., $\langle u_x^{2+}\rangle$) presented as the r.m.s. values (e.g., $u^+_{x\,rms} := \sqrt{\langle u_x^{2+}\rangle}$). The

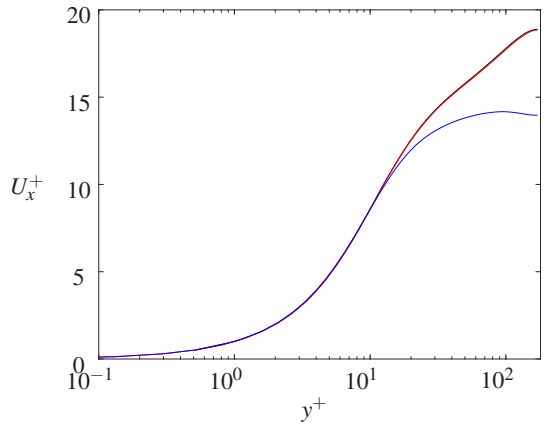

Figure 3: Mean velocity profile. Black line (non-swirling pipe **P0**). Red line (5% forcing **P5**). Blue line (50% forcing).

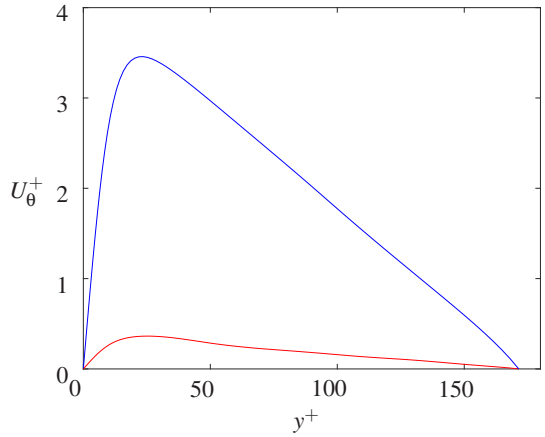

Figure 4: Mean swirl velocity profile. Red dashed line (5% forcing). Blue dashed line (50% forcing). Note that U_θ^+ is normalised by $u_{\tau,x}$.

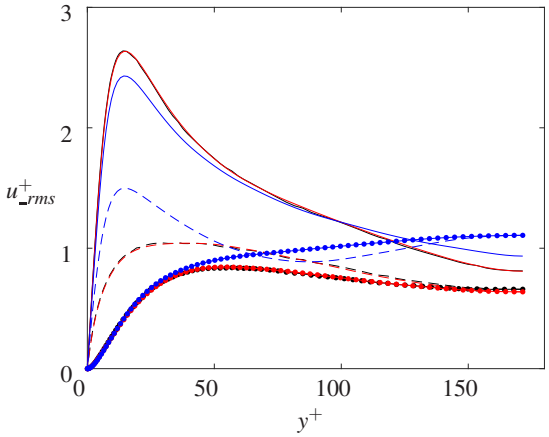

Figure 5: Turbulence intensities of swirling pipe flows compared to DNS straight pipe. Solid lines – $u^+_{x\,rms}$. Dot-dashed lines – $u^+_{r\,rms}$. Dashed lines – $u^+_{\theta\,rms}$. Colours: Black – straight pipe flow (**P0**); Red – 5% forcing (**P5**); and Blue – 50% forcing (**P50**).

lines correspond to: solid lines – $u^+_{x\,rms}$, dot-dashed lines – $u^+_{r\,rms}$ and dashed lines – $u^+_{\theta\,rms}$. For the lower swirl strength case **P5**, the r.m.s. for all three stresses collapse well with the non-swirling pipe flow. At the stronger swirl strength pipe flow case **P50**, It is observed that in the outer region all the three stresses show an increased magnitude. Interestingly, with increasing forcing only the streamwise velocity variance shows a reduction close to the wall, whereas the other two variances show an increase closer to the wall. It is possible that there is an energy transfer from the u_x-component to the other components close to the wall. Is also likely that this might be related to the 'thickening' of the streaks mentioned above, although a fuller analysis is required to confirm these speculations.

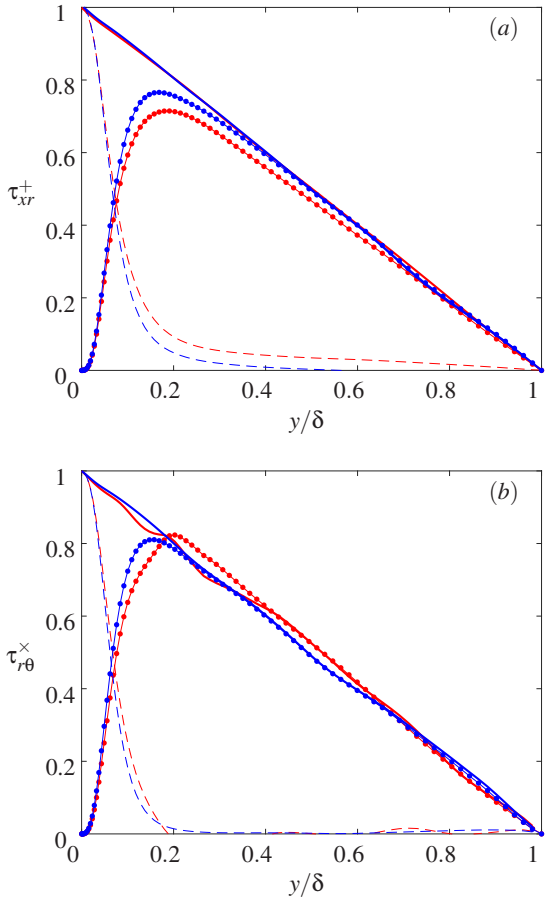

Figure 6: The total stresses Reynolds stress for cases **P5** (red) and **P50** (blue). (a) $\tau^+_{xr} = \frac{dU_x^+}{dy^+} - \langle u_r u_x \rangle^+$, solid lines – τ^+_{xr}, dot-dashed line – $\langle u_r u_x \rangle^+$ and dashed line – $\frac{dU_x^+}{dy^+}$. (b) $\tau^\times_{r\theta} = \left(\frac{dU_\theta^\times}{dy^\times} - \frac{U_\theta^\times}{y^\times}\right) - \langle u_r u_\theta \rangle^\times$, solid lines – $\tau^\times_{r\theta}$, dot-dashed line – $\langle u_r u_\theta \rangle^\times$ and dashed line – $\left(\frac{dU_\theta^\times}{dy^\times} - \frac{U_\theta^\times}{y^\times}\right)$.

Next, we investigated the normalised total stresses τ^+_{xr} and $\tau^\times_{r\theta}$, which are presented in figure 6. The total stresses are normalised by $u^2_{\tau,x}$ and $u^2_{\tau,\theta} \equiv \nu dU_\theta/dy|_{y=0}$ for τ^+_{xr} and $\tau^\times_{r\theta}$ respectively. Here the superscript $\times$ represents normalisation with ν and $u_{\tau,\theta}$. Figure 6(a) shows the total stress τ^+_{xr} for both swirling cases. Since there is not other external axial forcing being applied, the axial total stresses τ^+_{xr} for both swirling cases collapse well with the non-swirling pipe flow, which is as expected. When the τ^+_{xr} is further decomposed into the turbulent ($\langle u_r u_x \rangle^+$) and viscous ($\frac{dU_x^+}{dy^+}$) stresses, one would immediately notice an increase in the turbulent stress and decrease in the viscous stress. This is counter-intuitive as the turbulence intensities in the near-wall for the stronger swirl case $u^+_{x\,rms}$ is lower and the $u^+_{r\,rms}$ is somewhat similar (see figure 5), although $u^+_{\theta\,rms}$ is indeed higher. It is probably this decrease in viscous stress that allows the near-wall streaks to grow 'thicker'. Figure 6(b) shows the $\tau^\times_{r\theta}$ for both swirling cases. Here the $\tau^\times_{r\theta}$ are nor-

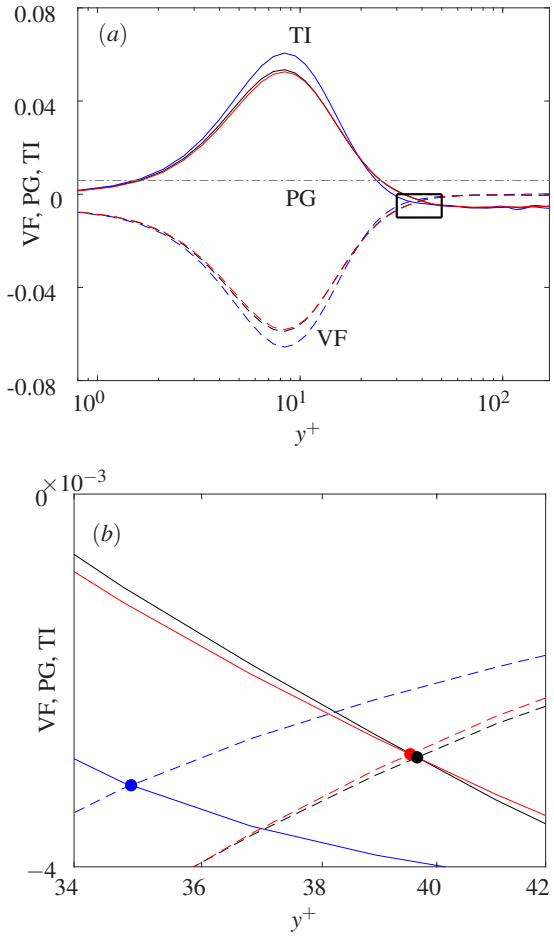

Figure 7: (a) Contribution of the pressure gradient (PG), viscous force (VF) and turbulent inertia (TI) to the mean momentum equation for all three cases. (b) Zoomed-in region of (a). Line colours are as in figure 3. The dots indicate the intercept of TI and VF.

malised by its respective $u_{\tau,\theta}$. It is interesting to note that the $\tau^{\times}_{r\theta}$ for both cases collapse and exhibit the exact linear slope as τ^{+}_{xr}. A decomposition of the $\tau^{\times}_{r\theta}$ is performed it appears that the turbulent and viscous stresses appears to collapse reasonably well. However, the figure 6(b) does show some lack of convergence, and would need to get more data obtain a better straight line.

Figure 7(a) shows the individual contributing terms of equation (1) for all three cases **P0, P5** and **P50**. Here it clearly shows that the TI and VF terms for the stronger swirl **P50** is greater in value compared to **P0** and **P5**. This increase in TI and VF for the stronger swirl case is analogous to a higher Reynolds number non-swirling pipe flow as report by [14], indicative of a more turbulent flow. A zoomed-in view (figure 7(a) black rectangle box) is shown in figure 7(b). The dots indicate the intercept of the VF and TI terms. The dots are in fact the start of region where the TI term is greater than the VF term, and is indicative of the start of the inertial regime or the logarithmic region. The wall-normal location y^+ of the intercept between VF and TI increases with Reynolds number [14]. However, for the stronger swirl case **P50**, the crossover (blue dot) is at a lower wall-normal y^+ location, which initially appears to have shifted to a lower Reynolds number pipe flow. This is not the case as the Reynolds number Re_τ is enforced to be the same for all three cases presented in figure 7(b). A lower y^+ intercept location means a larger physical logarithm and outer region, hence the higher swirl pipe flow behaves like a higher Reynolds number pipe flow, corresponding to a more 'turbulent flow'.

Conclusions

Direct numerical simulations of turbulent swirling pipe flows at two different swirl strengths are performed and compared with a non-swirling turbulent pipe flow. It is shown that at a swirl number of $S \approx 0.13$, there is a drag increase in the axial flow direction. All turbulence intensities at this swirl number exhibit an increase at the outer region of the pipe, indicating that swirling (at this particular S) leads to more turbulence. An investigation of the total stresses reveals that the streamwise and azimuthal friction velocities are appropriate for the scaling of the respective total stresses, more interesting, the stresses follow the equation $\tau_{xr} = \tau_{r\theta} = 1 - y/\delta$. The analysis of the axial mean momentum balance equation clearly shows an effect of adding swirl into the flow results in a more turbulent flow. The swirl reduces the viscous stress, which leads to 'thickening' of near-wall streaks. Future work will aim towards higher swirl number and higher Reynolds number simulations.

Acknowledgements

This work was supported with supercomputing resources provided by the Phoenix HPC service at the University of Adelaide. This research was also undertaken with the assistance of resources provided at the NCI NF through the National Computational Merit Allocation Scheme supported by the Australian Government. The authors acknowledge the financial support of the Australian Research Council.

References

[1] Blackburn, H. M and Sherwin, J. S., *J Comp. Phys.*, **197**, 2004, 759 – 778.

[2] Chin, C., Ng, H. C. H.,Blackburn, H. M., Monty, J. P. and Ooi, A., *Computers & Fluids*, **122**, 2015, (26-33).

[3] Chin, C., Ooi, A., Marusic, I. and Blackburn, H. M., *Phys. Fluids*, **22(11)**, 2010, (115107).

[4] Orlandi, P. and Fatica, M. *J Fluid Mech.* **343**, 43–72 (1997).

[5] Eggels, J. PhD thesis, Delft University of Technology, (1994).

[6] Zonta, F., Marchioli, C., and Soldati, A. *Int. J. Multiph. Flow* **56**, 172–183 (2013).

[7] Leclaire, B. and Jacquin, L. *J Fluid Mech.* **692**, 78–111 (2012).

[8] Facciolo, L., Tillmark, N., Talamelli, A., and Alfredsson, P. H. *Phys. Fluids (1994-present)* **19**(3), 035105 (2007).

[9] Kitoh, O. *J Fluid Mech.* **225** (1991): 445-479.

[10] Pierce, C. D. and Moin, P. *AIAA journal* **36**(7), 1325–1327 (1998).

[11] Nygard, F., and H. I. Andersson. *Int. J. Numer. Methods Fluids* **64**, no. 9 (2010): 945-972.

[12] Klewicki, J. C. *J Fluids Eng.* **132**, no. 9 (2010): 094001.

[13] Wei, T., P. Fife, J. Klewicki, and P. McMurtry. *J Fluid Mech.* **522** (2005): 303-327.

[14] Chin, C., J. Philip, J. Klewicki, A. Ooi, and I. Marusic. *J Fluid Mech.* **757** (2014): 747-769.

[15] Morrill-Winter, C, J. Philip, and J. Klewicki. *J Fluid Mech.* **813** (2017): 594-617.